Mechanically Driven Grain Boundary Formation in Nickel Nanowires

Lihua Wang,[†,‡] Deli Kong,[†] Yin Zhang,[§] Lirong Xiao,[†] Yan Lu,[†] Zhigang Chen,[‡] Ze Zhang,[†,||] Jin Zou,*[,‡,⊥] Ting Zhu,*[,§] and Xiaodong Han*[,†]

[†]Beijing Key Lab of Microstructure and Property of Advanced Material, Institute of Microstructure and Properties of Advanced Materials, Beijing University of Technology, Beijing 100124, China
[‡]Materials Engineering, The University of Queensland, Brisbane QLD 4072, Australia
[§]Woodruff School of Mechanical Engineering, Georgia Institute of Technology, Atlanta, Georgia 30332, United States
[||]Department of Materials Science, Zhejiang University, Hangzhou 310008, China
[⊥]Centre for Microscopy and Microanalysis, The University of Queensland, Brisbane QLD 4072, Australia

S *Supporting Information*

ABSTRACT: Metallic nanomaterials are widely used in micro/nanodevices. However, the mechanically driven microstructure evolution in these nanomaterials is not clearly understood, particularly when large stress and strain gradients are present. Here, we report the *in situ* bending experiment of Ni nanowires containing nanoscale twin lamellae using high-resolution transmission electron microscopy. We found that the large, localized bending deformation of Ni nanowires initially resulted in the formation of a low-angle tilt grain boundary (GB), consisting of randomly distributed dislocations in a diffuse GB layer. Further bending intensified the local plastic deformation and thus led to the severe distortion and collapse of local lattice domains in the GB region, thereby transforming a low-angle GB to a high-angle GB. Atomistic simulations, coupled with *in situ* atomic-scale imaging, unravelled the roles of bending-induced strain gradients and associated geometrically necessary dislocations in GB formation. These results offer a valuable understanding of the mechanically driven microstructure changes in metallic nanomaterials through GB formation. The work also has implications for refining the grains in bulk nanocrystalline materials.

Grain Boundary Formation Through Bending
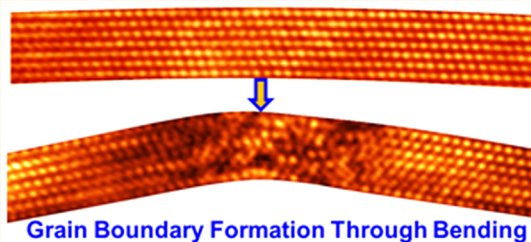
KEYWORDS: *in situ atomic-scale experiment, grain boundary formation, bending, geometrically necessary dislocations, lattice collapse*

Metallic nanomaterials often serve as load carrying components in micro/nanodevices. The reliability concerns of these devices call for a fundamental understanding of the mechanically driven microstructure evolution and damage in metallic nanomaterials. The past decade has witnessed dramatic advances in the nanomechanical characterization of metallic nanomaterials.[1−4] These studies are mostly conducted for uniaxial tension of nanowires[5,6] and uniaxial compression of nanopillars.[7,8] In these experiments, the overall stress and strain states are uniform throughout the cross sections of nanowires and nanopillars. As a result, it remains largely unknown regarding the effects of stress and strain gradients, resulting from nonuniform loads, on the mechanical behavior of nanomaterials. The atomic-scale mechanisms underpinning the nonuniform deformations in metallic nanomaterials remain elusive to date. On the other hand, since the discovery of nanocrystalline materials,[9] considerable effort has been devoted to studying the processing, structure and mechanical properties of these materials.[10−12] Mechanically driven grain refinement has been widely recognized as an effective approach for producing metallic nanocrystalline materials,[10−12] including for example various severe plastic deformation (SPD) techniques.[11] However, the atomic-scale mechanisms of grain refinement are not clearly understood, while extensive research has been conducted to investigate the grain subdivision mechanisms.[11,13−17] There is a critical lack of direct experimental observation of dynamic grain boundary (GB) formation at the atomic scale. Such *in situ* experiment is essential to understanding and improving the production of nanocrystalline materials.[18−20]

Here we conducted the *in situ* bending experiment of nanotwinned face-centered cubic (fcc) Ni nanowires (NWs) using high-resolution transmission electron microscopy (HRTEM). These Ni NWs had the initial diameters of ∼40 nm and contained the nanoscale growth twins. The long NWs under axial compression can be easily bent and are prone to form plastic hinges.

The resulting localized deformation of plastic bending can effectively facilitate the GB formation, yielding a finite misorientation between adjoining crystals.[21] Through a double-tilt loading stage, our TEM imaging revealed the real-time atomic processes of GB generation and evolution. We further combined HRTEM imaging and atomistic simulations to unravel the atomistic mechanisms of mechanically driven GB formation. We found that a low-angle tilt GB formed due to the accumulation of dislocations in a diffuse GB layer with finite width, in contrast to the atomically sharp GBs usually obtained from thermal annealing. With further bending, the localized plastic deformation was intensified in the GB region, leading to the transformation of a low-angle GB into a high-angle GB through distortion and collapse of local lattice domains. We also observed the dynamic GB recovery which reversed the disordered to ordered domains in the GB region. Our atomistically resolved results provide valuable insights into the mechanically driven GB formation.

RESULTS AND DISCUSSION

The nanotwinned Ni NWs used in this work were synthesized by electrochemical deposition. These NWs had the axial orientation of <112>, initial length of ∼50 μm and diameter of ∼40 nm. Figure 1A shows an overview image of a Ni NW and Figure 1B shows the selected area electron diffraction (SAED) pattern of this NW captured along the [$\bar{1}$10] zone axis. The SAED pattern consists of two sets of <110> diffraction patterns with a common <111> diffraction spot, indicating the presence of {111} twins in the NW. Figure 1C shows an HRTEM image of nanoscale twin lamellae in the NW, thus confirming the presence of {111} twins. Our HRTEM observations indicated that the twin thicknesses varied in the range of 1−14 nm. The {111} TBs were atomically flat and parallel to the longitudinal section of the NW. The NWs contained no visible dislocations.

We conducted the *in situ* bending tests of individual nanotwinned Ni NWs by using a recently developed loading method inside TEM.[22−24] Figure 2 highlights the most salient deformation characteristics in the bending tests, and the corresponding detailed analysis will be provided in succeeding figures. The low-magnification TEM images in Figure 2A−D show the gradually increased bending deformation in the Ni NW. A small, uniform elastic bend was initially generated throughout the NW (Figure 2A). According to the classical beam theory, the

maximum bending strain (ε_b) occurs at the top and bottom surfaces of a bent beam and can be expressed as $\varepsilon_b = r/R$[25] (where R denotes the bending radius of curvature of the neutral plane and r denotes the radius of the NW). We estimated ε_b as ∼1.9% for the bent NW in Figure 2A. Upon further bending, the large plastic deformation occurred predominantly within a local region of the NW, forming a plastic hinge (Figure 2B). Subsequently, the domain of this plastic hinge expanded (Figure 2C), resulting in the formation of two high-angle tilt GBs about the out-of-plane [011] direction (Figure 2D). Each of the two high-angle GBs produced an abrupt change of the tilt angle of ∼20° between a short middle segment and a long arm of the NW.

Figure 2E−H presents a sequence of HRTEM images showing the atomic-scale deformation near a (111) TB in the NW. This TB was initially flat and marked by a long red line in Figure 2E. It became increasingly curved with increasing bend of the NW (Figure 2F−H). The fcc lattices on the two sides of the TB retained mirror symmetry, as indicated by the short red segments representing the respective inclined {111} planes above and below the TB. During the formation of high-angle GBs, the local lattice near the GB region became highly distorted and even disordered. Figure 2I shows a representative HRTEM image near a bending-deformation induced tilt GB when the tilt angle reached ∼21.5° between adjoining crystals. In this image, the lattice became highly disordered in the GB region having a thickness of ∼2 nm. It was previously suggested that GBs could form via a dislocation or a disclination-dipole mechanism (see Figure S1−S3 in Supporting Information). However, our *in situ* experiments revealed that the GB formed initially through a dislocation-mediated process and subsequently by lattice disordering and recovery, as shown in detail below.

To reveal the atomic-scale dynamic processes of GB formation, Figure 3 shows a sequence of HRTEM images taken around a ∼ 6.8 nm thick twin (corresponding to the green boxed region in the inset of Figure 3A). Figure 3A presents a typical HRTEM image when plastic deformation just started in the bent NW. At this stage, some full dislocations were randomly distributed in the NW. With increasing bend, the (111) lattice planes parallel to the longitudinal section of the NW became increasingly curved (Figure 3B). Meanwhile, an increasing number of dislocations was accumulated in the NW. In Figure 3C, a low-angle GB formed with a tilt angle of ∼12.1°. Hereafter we term the low-angle and high-angle GB in terms of the tilt angle smaller than

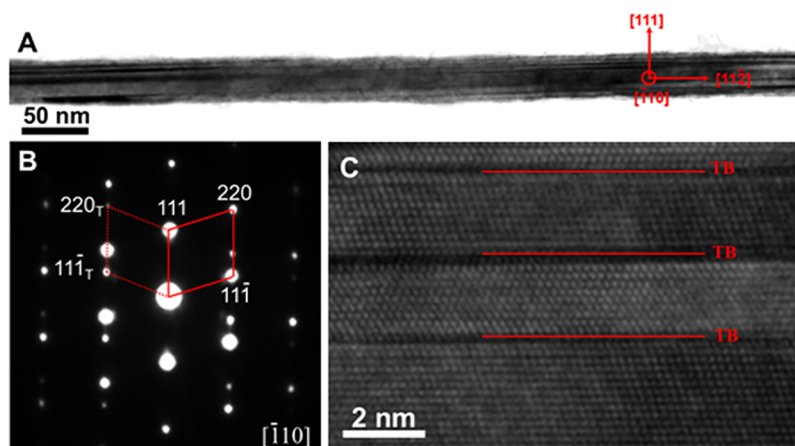**Figure 1.** Initial microstructure of a nanotwinned Ni NW. (A) TEM image showing the overall morphology of a < 112>-oriented Ni NW. (B) SAED pattern indicating the presence of {111} twins in the NW. (C) HRTEM image showing several twin boundaries (TBs) in the Ni NW.
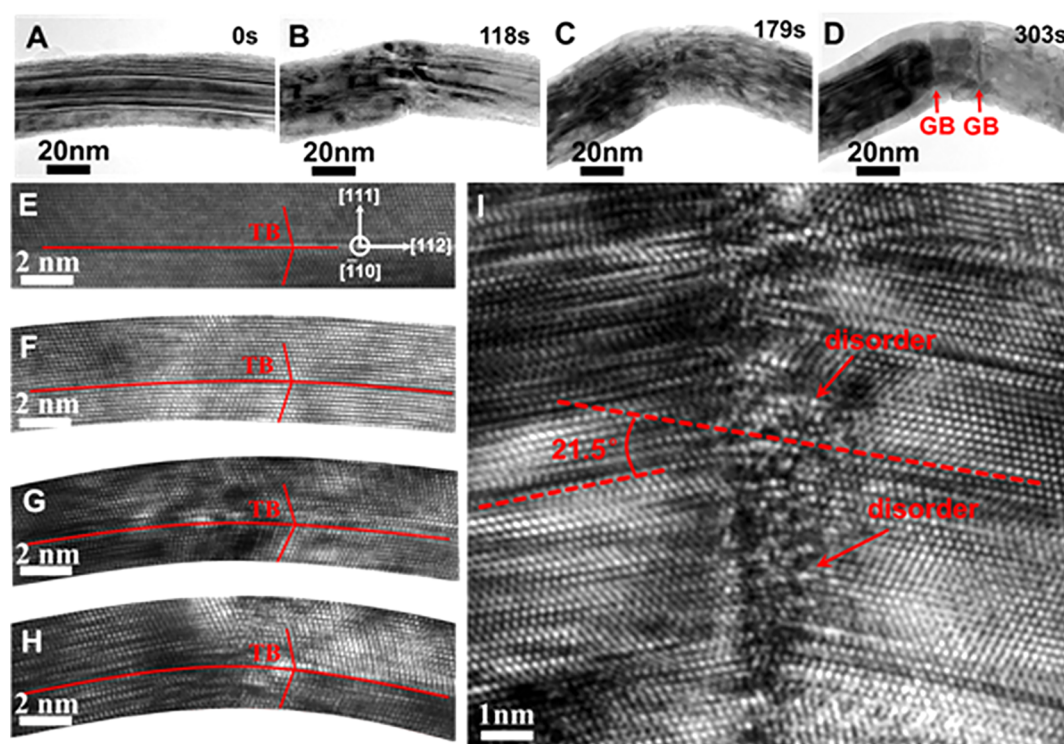
Figure 2. *In situ* atomic-scale observation of plastic bending deformation in a nanotwinned Ni NW. (A−D) TEM images showing the characteristic bending processes, including (A) elastic bend throughout the NW, (B) formation of a sharply bent region, namely, a localized plastic hinge, (C) expansion of the plastic hinge, and (D) formation of two GBs. (E−H) HRTEM images showing the atomic-scale lattice deformation near a TB with increasing bend of the NW. The long red line represents a TB and the short red lines represent the inclined {111} slip planes. (I) A representative HRTEM image showing the disordered lattice in a diffuse layer of a symmetrical high-angle GB with the tilt angle of 21.5°.
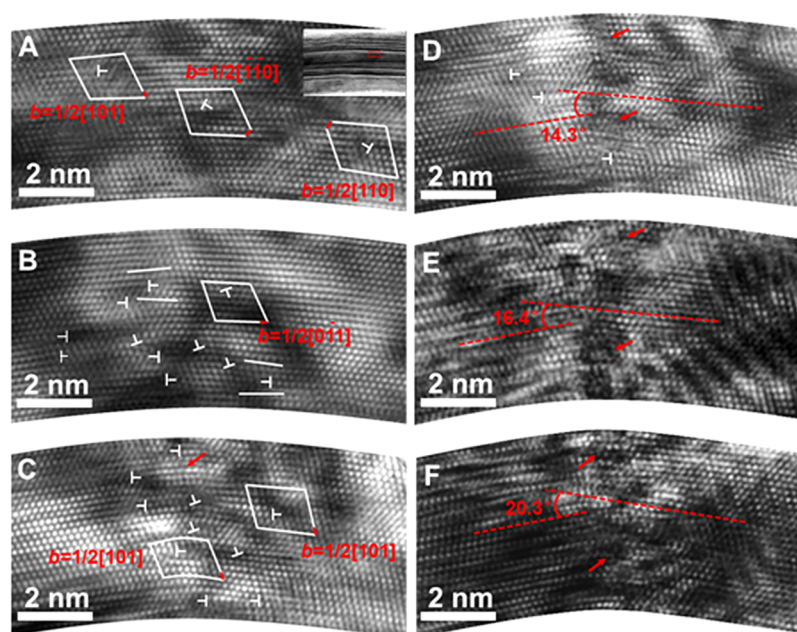

Figure 3. *In situ* HRTEM images showing the formation of a high-angle tilt GB around a thick twin. (A) HRTEM image captured when plastic bending deformation just started, and several full dislocations were randomly distributed (marked by the symbol of ⊥) in the bent lattice. This HRTEM image corresponds to the green-boxed region in the inset. (B−C) The increasing load resulted in more full dislocations. (D) A low-angle GB with the tilt angle of ~14.3° was generated; the original parallelogram shaped lattice became largely distorted in the diffuse layer of the GB. (E) The lattice collapse and disordering occurred in the local domains (indicated by arrows) in the GB region, as the GB tilt angle was increased to ~16.4°. (F) The fraction of the disordered domains in the GB region increased as the GB tilt angle reached 20.3°.

and greater than 15°, respectively. Such a mechanically induced GB consisted of randomly distributed dislocations in a diffuse GB

layer, which clearly contrasted with the low-energy tilt GB configuration that forms via thermal annealing and thus consists of a
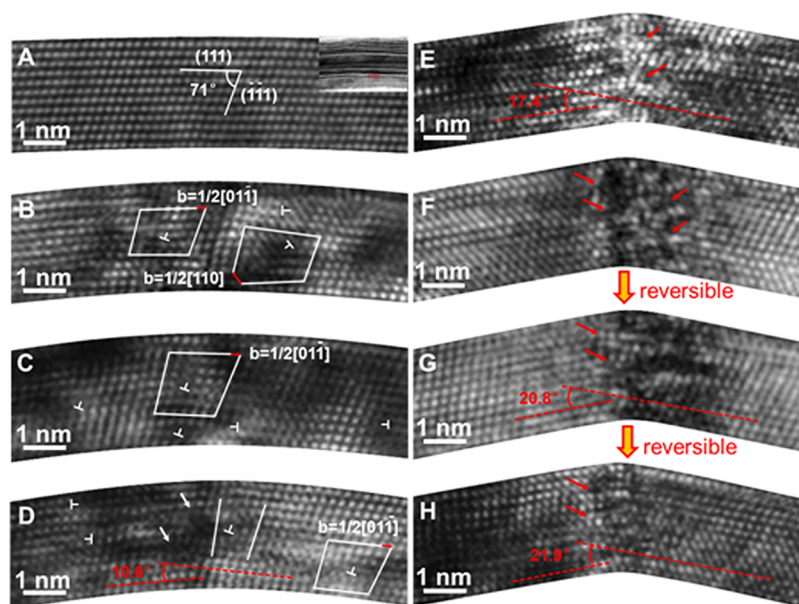
Figure 4. *In situ* HRTEM images showing the formation of a high-angle tilt GB similar to that in Figure 3, but revealing a valuable phenomenon of dynamic recovery in the GB region. (A) HRTEM image showing the elastically bent lattice. This HRTEM image corresponds to the green-boxed region in the inset. (B,C) An increasing number of full dislocations (marked by the symbol of ⊥) formed with increasing bend of the NW. (D) A low-angle GB with the tilt angle of ~10.6° was generated. The domains with large lattice distortion were marked by arrows. (E) Lattice collapse and disordering occurred in the GB region, leading to the formation of a high-angle GB with the tilt angle of 17.4°. (F) Formation of the high-angle GB was accompanied by the flattening of the bent (111) lattice planes on the two sides of the GB. (G,H) Further bending led to the mechanically induced recovery of the disordered domains back to the order crystalline domains in the GB region.

sharp "wall" of edge dislocations of the same sign regularly arranged one above another. The dislocation density reached 4×10^{15} μm^{-2} in the GB region. The randomly distributed dislocations generated a highly nonuniform strain field, manifested by a nonuniform lattice fringe pattern. Upon further bending, the GB tilt angle was increased to ~14.3° (Figure 3D). A detailed analysis was given to the GB structure by tracking the atomic positions in the HRTEM images (Figure S4). It is seen that the original parallelogram-shaped lattice cells became highly distorted, but no regularly arranged dislocation arrays could be identified in the GB region. Such large lattice distortion led to lattice collapse and disordering in the local cells. As a result, a symmetric high-angle GB formed with the tilt angle of ~16.4° in Figure 3E and ~20.3° in Figure 3F. Correspondingly, the fraction of disordered domains in the GB region increased with increasing tilt angle. Hence, the HRTEM images in Figure 3 reveal a mechanically driven atomic process of high-angle GB formation through lattice bending, dislocation nucleation and accumulation, large lattice distortion and disordering in a diffuse GB layer about a few nanometer thick.

Figure 4 presents a different set of HRTEM images showing a similar process of formation of a symmetric high-angle GB as in Figure 3. Interestingly, a phenomenon of lattice recovery was uncovered during GB formation. Figure 4A shows an HRTEM image taken from the green boxed region in the inset. In this image, the lattice bending was uniformly elastic. Figures 4B−C show the plastic bending responses, featuring an increasing number of dislocations with increasing bend of the NW. Figure 4D shows the formation of a low-angle GB with the tilt angle of ~10.6°. The diffuse GB region contained a mix of randomly distributed dislocations and disordered domains of collapsed lattice (marked by arrows). As the GB tilt angle was increased to ~17.4° (Figure 4E), the disordered domains had spread throughout the GB region. Notably, the formation of such

a high-angle GB was accompanied by the flattening of the elastically bent (111) lattice planes on the two sides of the GB, as seen in Figure 4F. This indicates a substantial release of elastic bending energies in the adjoining crystals across the GB. Interestingly, upon further bending of the NW, the GB region underwent a dynamic recovery process associated with the reverse transformation of the disordered domains to the regular fcc lattice domains, as shown in Figure 4G−H. The dynamic recovery was driven by both the applied mechanical load and the volume difference between amorphous and crystalline phases. It thus corresponded to a "mechanical annealing" process. As a result, the high-energy disordered domains in the GB region were transformed to the low-energy ordered domains.[26−28] Such a recovery process occurred at the large GB tilt angles (*e.g.*, 20.8° in Figure 4G and 21.9° in Figure 4H). It signified a large energy release in the GB region, resulting in a more stable high-angle GB with major lattice domains.

Similar to the previous case of GB formation in thick twins, we also observed the GB formation in thin twins through lattice bending, dislocation nucleation and accumulation, large lattice distortion and disordering. However, these processes in thin twins were frequently mediated by partial dislocations, and more strongly influenced by TBs than in thick twins. Figure 5A shows an HRTEM image around a thin twin of ~2.8 nm thick (corresponding to the boxed region in the inset), when plastic deformation just started. In contrast to the dominant operation of full dislocations in thick twins (Figures 3 and 4), partial dislocations and stacking faults (marked by arrows) served as major carriers of plastic deformation in thin twins. That is, plastic bending deformation was primarily accommodated by an increasing amount of stacking faults in conjunction with large bending of the (111) lattice planes including TBs. As shown in Figure 5B, a low-angle GB with the tilt angle of ~14.6° was generated by partial dislocations and stacking faults. With an
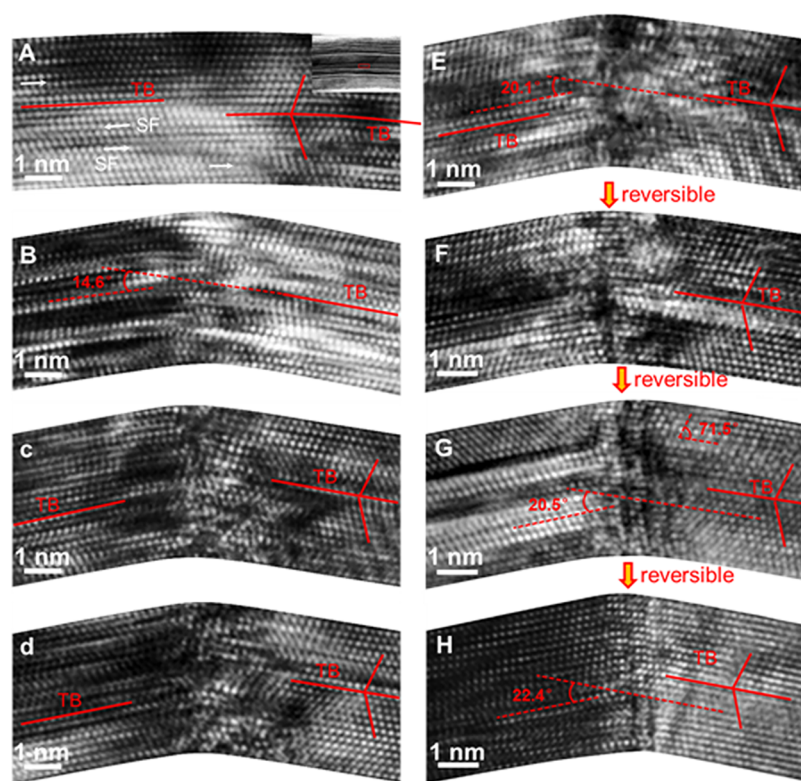
Figure 5. *In situ* HRTEM images showing the formation of a high-angle tilt GB around a thin twin. (A) HRTEM image captured when plastic bending deformation just started. Several partial dislocations and stacking faults (SFs) were observed and marked by arrows. This HRTEM image corresponds to the green-boxed region in the inset. (B) A low-angle GB formed with the tilt angle of ~14.6°. (C−E) The lattice became increasingly disordered in the diffuse GB region, resulted in the formation of a symmetric high-angle GB with the tilt angle of 20.1° in (E). (F,G) The disordered domains in the GB region recovered to the ordered crystalline domains. (H) Most of the GB region became the ordered lattice when the GB tilt angle reached ~22.4°.

increasing bend of the NW, the lattice became disordered in the GB region (Figure 5B and D). This led to the formation of a symmetric high-angle GB with a tilt angle of 20.1° (Figure 5E). Similar to the formation of high-angle GBs in thick twins, the disordered domains at the GB recovered to the ordered crystalline domains as the NW bend continued to increase (Figure 5F and G). Figure 5H shows that the tilt angle of the high-angle GB reached ~22.4° and most of the GB region became ordered with a clearly visible lattice.

To further understand the atomistic mechanisms of GB formation in experiments, we performed molecular dynamics (MD) simulations of plastic bending in a nanotwinned Ni NW. In contrast to uniaxial deformation, plastic bending features the generation of gradient plastic strains,[29−31] which can be accommodated by the so-called geometrically necessary dislocations (GNDs), *i.e.*, dislocations of the same sign.[32] Here we combined MD simulations and HRTEM results to investigate the bending-induced GNDs and associated GB formation processes.

Figure 6A and B show the representative MD snapshots of bending-induced dislocations in a plastically bent Ni NW. As shown in Movie S1, dislocations nucleated from the top and bottom surfaces of the bent NW, and then transmitted across TBs into internal twin lamellae. With the double Thompson tetrahedral representing all the possible {111}⟨110⟩ slip systems of dislocations in twin lamellae, Figure 6C highlights the most favorable modes of slip transfer across a TB, namely, direct transmission of screw dislocations with the Burgers vectors of the $\vec{b}_1$ type (indicated by thick pink arrows), which are along the

⟨110⟩ slip directions in the TB.[33] Dislocations in Figure 6A and B (marked by red and green circles) have this type of Burgers vector $\vec{b}_1$.

The generation and evolution of dislocations during plastic bending are clearly represented by the processes of surface nucleation, slip transmission and cross-slip of a screw dislocation (Figure 6D−F). Specifically, during the bending of the NW, a screw dislocation with the Burgers vector $\vec{b}_1$ nucleated from the top surface and then transmitted across the TB. It subsequently cross-slipped from the inclined {111} slip plane onto the horizontal (111) slip plane parallel to the TB (Figure 6D); a snapshot of the cross-slip process is shown in Figure 6E. After cross-slip, this screw glided to the incipient GB region in the middle of the NW for accommodating the increasing bend therein. Interestingly, the dislocation line adjusted its orientation to align with the $[\bar{1}10]$ tilt axis of the incipient GB, such that it became the mixed 60° type (Figure 6F). The Burgers vector $\vec{b}_1$ of this 60° dislocation has a resolved shear displacement component in the $[11\bar{2}]$ axial direction of the NW. This explains why it tends to move to the incipient GB region, so as to serve as a GND for accommodating the lattice misorientation across the GB or equivalently for generating the local plastic strain gradient in the NW. For the tilt GB produced in both MD simulations and TEM experiments, the lattice symmetry condition on the two sides of the GB led to the alignment of the dislocation line with the $[\bar{1}10]$ tilt axis of the GB. Similarly, another 60° dislocation (marked by a green circle in Figure 6B) was also generated through a series of processes including surface nucleation, slip
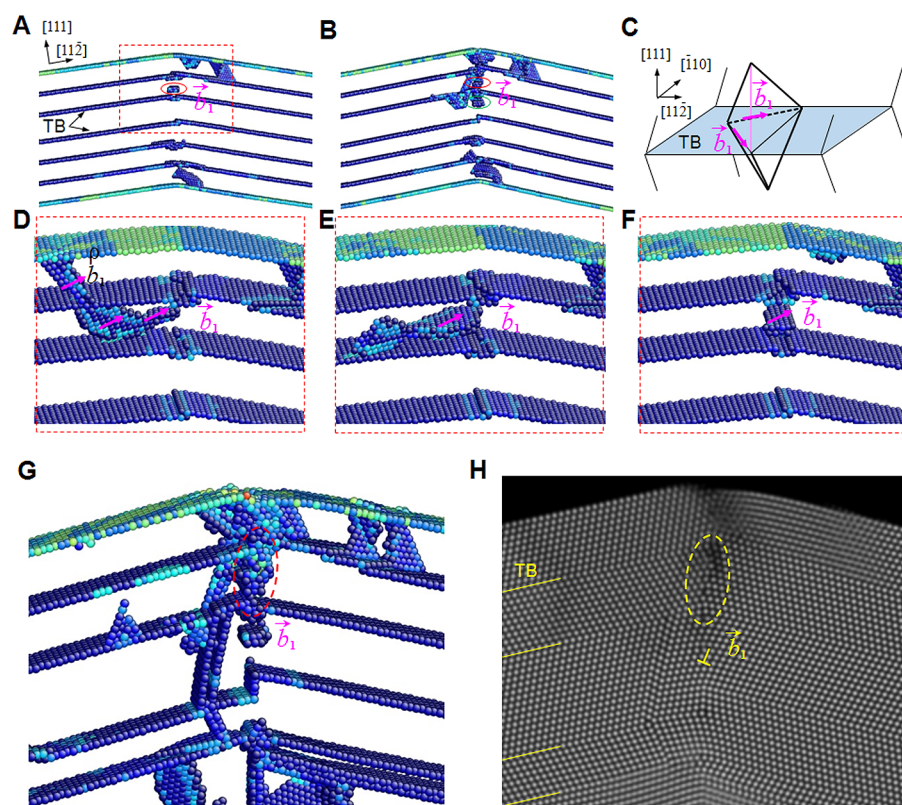
Figure 6. MD simulation of plastic bending and GB formation in a nanotwinned Ni NW. (A,B) MD snapshots showing a local region undergoing large plastic bending deformations, thereby forming an incipient GB. Plastic deformation occurring in the incipient GB region involved dislocation nucleation from NW surfaces, as well as dislocation migration across and within twin lamellae. (C) Schematic of a double-Thompson tetrahedron representing all the possible {111}⟨110⟩ slip systems in twin lamellae. Screw dislocations in (A,B) (marked by red and green circles) have the Burgers vector of the $\vec{b}_1$-type, such that they can transmit across the TB most easily. (D−F) Magnified MD snapshots showing the detailed dislocation process that occurred in the boxed region in (A), including dislocation transmission across a TB, subsequent cross-slip within a twin lamella, and alignment of dislocation line along the [$\bar{1}$10] tilt axis of the GB, thus forming a 60° dislocation. (G) A MD snapshot showing formation of a high-angle GB consisting of highly dense dislocation junctions (marked by a red circle). (H) Simulated HRTEM image using the atomic structure in (G). The circle region shows the largely distorted and even locally disordered lattice, which corresponds to the highly dense dislocation junctions in (G).

transmission, cross-slip, and alignment with the [$\bar{1}$10] tilt axis of the incipient GB. Since dislocations of the $\vec{b}_1$-type are GNDs that can easily transmit across the TB, their generation and accumulation contributed substantially to GB formation in the plastically bent nanotwinned NW. It is important to emphasize that our HRTEM imaging was taken along the [$\bar{1}$10] tilt axis of the GB (*i.e.*, direction of the 60° dislocation line). Hence full dislocations captured in HRTEM images should be of the same 60° type as those in MD simulations. The presence of a high density of 60° dislocations in HRTEM images, particularly within thick twins, underscored the important role of these 60° dislocations in the formation of tilt GBs during *in situ* bending experiments.

As shown in Figure 6G, further bending of the NW resulted in the accumulation of dislocations in the GB region, and these 60° dislocations also formed sessile junctions with dislocations on inclined slip planes. Figure 6H shows a simulated HRTEM image of the atomic configuration in Figure 6G. Large distortion and disordering of the local lattice domains as circled in Figure 6H are associated with the highly dense dislocation junctions in Figure 6G. This result suggests that dislocation accumulation and junction formation could underlie the disordering processes in the GB region during bending experiments. Correspondingly, the recovery process observed through

HRTEM imaging was likely caused by the mechanically induced relaxation of dislocation configurations as well as the disruption of dislocation junctions. Finally, we note that with increasing bend, dislocations other than the $\vec{b}_1$-type were also activated in MD simulations. These dislocations reacted with TBs through absorption, desorption and direct transmission,[33] thereby producing TB steps. These steps glided along TBs, causing TB migration; they also served as sources to emit dislocations into twin lamellae. These TB partial-mediated processes also contributed to the GB formation, as observed during HTREM imaging, particularly in thin twins.

Previous studies suggested that GBs could form through the generation of dislocation arrays or disclination dipoles. Most experiments of GB formation were conducted for relatively large bulk samples, such that the atomistic mechanisms of GB formation could not be clearly resolved in real time. Recent investigation reported an interesting *in situ* TEM bending tests of submicrometer-sized single-crystal Al pillars.[34] Their postmortem HRTEM imaging indicated that the low-angle GBs, which formed during bending tests, consisted of dislocation arrays, but the dislocation type and arrangement could not be clearly resolved. On the other hand, the past decade has seen a dramatic increase in nanomechanical testing of nanopillars[35] and nanowires.[5,36,37] However, the applied load was usually uniaxial

compression or tension, which produced the dominantly uniform stresses and strains in nanopillars and nanowires. Hence, there is a lack of necessary lattice bending and resultant plastic strain gradients for driving the GB formation.[38−41] In addition, twinning and phase transformation often dominated over dislocation plasticity in those studies,[8] thus making it difficult to observe the dislocation-mediated GB formation. In this work, plastic bending of Ni NWs produced severe plastic strain gradients for creating GNDs and thus driving the GB formation.

CONCLUSIONS

Our *in situ* HRTEM imaging directly revealed the atomic processes of mechanically induced GB formation. Two different mechanisms of GB formation were uncovered. The first mechanism involved the nucleation and migration of dislocations, resulting in the generation of low-angle GBs. Such kind of mechanically induced GB consisted of randomly distributed dislocations in a diffuse GB layer, which contrasted with the thermally annealed (tilt) GB consisting of a sharp "wall" of regularly arranged edge dislocations. The second mechanism involved the severe distortion and collapse of local lattice domains in the low-angle GB region, thereby resulting in a high-angle GB consisting of disordered domains. Further bending of the NW even triggered dynamic recovery in the GB, reversing the disordered domains to the ordered lattice domains. Our atomistic simulations revealed the atomic processes of lattice distortion and collapse resulting from the interlocking and junction formation of dislocations. Atomistic simulations also showed the dynamic recovery due to mechanically induced relaxation of dislocation configurations and disruption of dislocation junctions. In contrast to previous GB formation mechanisms, no disclination dipoles or regularly rearranged dislocation arrays were observed during *in situ* HRTEM experiments.

It should be noted that the small-volume NWs tended to experience a dislocation-starved condition during plastic deformation,[35] such that they required the surface nucleation of dislocations to initiate and sustain plastic bending. Such surface nucleation-controlled plastic deformation could be different from the dislocation processes in SPD-processed bulk crystals, which contain plenty of dislocation sources in large-sized grains. However, the TBs (*i.e.*, $\sum 3$ GBs) in the present nanotwinned NWs serve as strong obstacles to the propagation of surface-nucleated dislocations.[42,43] These TB-mediated dislocation processes, along with severe plastic bending deformation in the GB-forming region, can create the sufficiently complicated deformation geometries and local stress states that could adequately resemble those in SPD-processed bulk crystals. Hence, the mechanisms of GB formation through severe lattice bending, as uncovered by the present *in situ* TEM experiments, provide valuable insights into the mechanically induced formation of tilt GBs in bulk polycrystalline materials. It is worth noting that the confining pressure is different between the NW bending and SPD processing. Hence, the pressure effects on the mechanism of GB formation warrant further study in the future.

METHODS

***In Situ* TEM Experiment.** The *in situ* bending tests of individual NWs were conducted using our recently developed method.[22−24] The NWs were scattered on a broken TEM grid, which was covered by colloidal thin films. Second, the grid was placed in a conventional TEM specimen holder. Under electron beam irradiation, the scattered NWs could then be bent by the colloidal thin films at low strain rates ($\sim 10^{-4}$/s). Using this technique, the specimen could be tilted along two

orthogonal directions by large angles of $\pm 20°$ without the need for a special specimen holder or mechanical tensile attachment. Along a selected crystallographic direction, the bending or axial tensile deformation of individual NWs can be recorded *in situ* at the atomic scale. The experiments were performed using a JEOL high-resolution TEM with a field-emission gun (JEOL 2010 F). The point resolution was 0.19 nm.

Atomistic Modeling. We performed molecular dynamics simulations of plastic bending of a nanotwinned Ni nanowire (NW) using LAMMPS with an embedded-atom method potential.[44] The simulated sample is a 684 nm × 126 nm × 84 nm nanowire, containing five equally spaced (111) twin boundaries, as shown in Figure S5. Each twin lamella has a thickness of 21 nm. The system contains 368 640 atoms in total. Since MD simulation is limited by the accessible time scale, it is formidable to directly simulate the entire bending process in the NW as *in situ* TEM experiment. Hence, we devised the MD loading scheme to simulate a three-point bending process, such that the distributed lateral forces was applied in a local region of the nanotwinned Ni NW. This facilitated the generation of a plastic hinge in the NW, thereby resulting in a symmetric tilt GB similar to experiment. Specifically, the orange boxed region in Figure S5 is 10 nm wide in the *x*-direction and contains 5382 atoms. The green boxed region is 60 nm wide and contains 32000 atoms. To simulate the three-point bending process, we relaxed the free-standing NW by conjugate gradient (CG) energy minimization. Then we applied a three-point bending load to the NW. That is, the atoms in the green boxes were fixed in the *y*-direction. A linear spring was attached between the atoms in the orange box and a reference point away from the NW using the fix modify command in LAMMPS. The spring energy was minimized when the atoms in the orange box coincide with the reference point. As a result, the beam started to bend, as the system was relaxed at a low temperature of 1 K. We have obtained similar MD results at 300 K as well as for thicker twin lamellae (*e.g.*, with the twin thickness up to 32 nm).

ASSOCIATED CONTENT

Ⓢ **Supporting Information**

The Supporting Information is available free of charge on the ACS Publications website at DOI: 10.1021/acsnano.7b06605.

> The *in situ* atomic-scale observation of GB formation through dislocation arrays created disclination dipoles; a 6 nm × 11 nm sized subgrain with a GB angle of ~10° formed through dislocation mechanisms; two sets of {111} lattice fringes show that no dislocation arrays were observed when the lattice misorientation across the incipient GB was ~9.6°; *in situ* observation of the original parallelogram-shaped lattice became irregular; and schematic illustration of molecular dynamics simulation of plastic bending of a nanotwinned Ni NW (PDF)
>
> Movie of molecular dynamics simulations of plastic bending of a nanotwinned Ni nanowire, resulting in the formation of in a nearly symmetric tilt GB similar to the bending-induced GBs observed during *in situ* TEM experiments (AVI)

AUTHOR INFORMATION

Corresponding Authors
*E-mail: j.zou@uq.edu.au.
*E-mail: ting.zhu@me.gatech.edu.
*E-mail: xdhan@bjut.edu.cn.

ORCID Ⓞ
Xiaodong Han: 0000-0002-0193-1291

Author Contributions
L.H.W. conducted the *in situ* TEM experiments. L.H.W., D.L.K., L.R.X., T.J.X., and Y.L. analyzed the experimental results. X.D.H., Z.Z., and J.Z. designed the project and guided the research. Y.Z.

and T.Z. performed atomistic simulations. L.H.W., T.Z., X.D.H., and J.Z. wrote the manuscript. All authors contributed to the extensive discussion of the results.

Notes

The authors declare no competing financial interest.

REFERENCES

(1) Zhu, T.; Li, J. Ultra-Strength Materials. *Prog. Mater. Sci.* **2010**, *55*, 710−757.

(2) Greer, J. R.; De Hosson, J. T. M. Plasticity in Small-Sized Metallic Systems: Intrinsic *Versus* Extrinsic Size Effect. *Prog. Mater. Sci.* **2011**, *56*, 654−724.

(3) Legros, M.; Gianola, D. S.; Motz, C. Quantitative *In Situ* Mechanical Testing in Electron Microscopes. *MRS Bull.* **2010**, *35*, 354−360.

(4) Kraft, O.; Gruber, P. A.; Monig, R.; Weygand, D. Plasticity in Confined Dimensions. *Annu. Rev. Mater. Res.* **2010**, *40*, 293−317.

(5) Chen, L. Y.; He, M.-R.; Shin, J.; Richter, G.; Gianola, D. S. Measuring Surface Dislocation Nucleation in Defect-Ccarce Nanostructures. *Nat. Mater.* **2015**, *14*, 707−713.

(6) Zhu, Y. Mechanics of Crystalline Nanowires: An Experimental Perspective. *Appl. Mech. Rev.* **2017**, *69*, 010802.

(7) Uchic, M. D.; Dimiduk, D. M.; Florando, J. N.; Nix, W. D. Sample Dimensions Influence Strength and Crystal Plasticity. *Science* **2004**, *305*, 986−989.

(8) Wang, J.; Zeng, Z.; Weinberger, C. R.; Zhang, Z.; Zhu, T.; Mao, S. X. *In Situ* Atomic-Scale Observation of Twinning-Dominated Deformation in Nanoscale Body-Centred Cubic Tungsten. *Nat. Mater.* **2015**, *14*, 594−600.

(9) Gleiter, H. Nanocrystalline Materials. *Prog. Mater. Sci.* **1989**, *33*, 223−315.

(10) Valiev, R. Materials science: Nanomaterial Advantage. *Nature* **2002**, *419*, 887−889.

(11) Valiev, R. Z.; Islamgaliev, R. K.; Alexandrov, I. V. Bulk Nanostructured Materials from Severe Plastic Deformation. *Prog. Mater. Sci.* **2000**, *45*, 103−189.

(12) Wang, L. H.; Zhang, Z.; Han, X. D. *In Situ* Experimental Mechanics of Nanomaterials at the Atomic Scale. *NPG Asia Mater.* **2013**, *5*, e40.

(13) Estrin, Y.; Vinogradov, A. Extreme Grain Refinement by Severe Plastic Deformation: A Wealth of Challenging Science. *Acta Mater.* **2013**, *61*, 782−817.

(14) Hughes, D. A.; Hansen, N. High Angle Boundaries Formed by Grain Subdivision Mechanisms. *Acta Mater.* **1997**, *45*, 3871−3886.

(15) Imayev, R. M.; Imayev, V. M.; Salishchev, G. A. Formation of Submicrocrystalline Structure in TiAl Intermetallic Compound. *J. Mater. Sci.* **1992**, *27*, 4465−4471.

(16) Li, B. L.; Godfrey, A.; Liu, Q. Subdivision of Original Grains During Cold-Rolling of Interstitial-Free Steel. *Scr. Mater.* **2004**, *50*, 879−883.

(17) Svyetlichnyy, D. S.; Muszka, K.; Majta, J. Three-Dimensional Frontal Cellular Automata Modeling of the Grain Refinement During Severe Plastic Deformation of Microalloyed Steel. *Comput. Mater. Sci.* **2015**, *102*, 159−166.

(18) Han, X. D.; Zhang, Y. F.; Zheng, K.; Zhang, X. N.; Zhang, Z.; Hao, Y. J.; Guo, X. Y.; Yuan, J.; Wang, Z. L. Low-Temperature *In Situ* Large

Strain Plasticity of Ceramic SiC Nanowires and Its Atomic-Scale Mechanism. *Nano Lett.* **2007**, *7*, 452−457.

(19) Wang, L. H.; Zheng, K.; Zhang, Z.; Han, X. D. Direct Atomic-Scale Imaging About the Mechanisms of Ultralarge Bent Straining in Si Nanowires. *Nano Lett.* **2011**, *11*, 2382−2385.

(20) Kisel, V. P. Mechanism of Formation and Mechanical Behavior of Tilt Grain Boundaries. *Phys. Stat. solid. A* **1995**, *149*, 61−68.

(21) Cottrell, A. H. *Dislocations and plastic flow in crystals*; Oxford University Press: London, 1953.

(22) Zheng, K.; Wang, C. C.; Cheng, Y. Q.; Yue, Y. H.; Han, X. D.; Zhang, Z.; Shan, Z. W.; Mao, S. X.; Ye, M.; Yin, Y.; Ma, E. Electron-Beam-Assisted Superplastic Shaping of Nanoscale Amorphous Silica. *Nat. Commun.* **2010**, *1*, 1.

(23) Han, X. D.; Zheng, K.; Zhang, Y. F.; Zhang, X. N.; Zhang, Z.; Wang, Z. L. Low-Temperature *In Situ* Large-Strain Plasticity of Silicon Nanowires. *Adv. Mater.* **2007**, *19*, 2112−2118.

(24) Wang, L. H.; Kong, D. L.; Xin, T. J.; Shu, X. Y.; Zheng, K.; Xiao, L. R.; Sha, X. C.; Lu, Y.; Zhang, Z.; Han, X. D.; Zou, J. Deformation Mechanisms of Bent Si Nanowires Governed by the Sign and Magnitude of Strain. *Appl. Phys. Lett.* **2016**, *108*, 151903.

(25) Landau, L. D.; Kosevich, A. M. *Theory of Elasticity*, 3rd ed.; Butterworth-Heinemann: Oxford, 1986.

(26) Komanduri, R.; Chandrasekaran, N.; Raff, L. M. Molecular Dynamics (MD) Simulation of Uniaxial Tension of Some Single-Crystal Cubic Metals at Nanolevel. *Int. J. Mech. Sci.* **2001**, *43*, 2237−2260.

(27) Zhong, L.; Wang, J.; Sheng, H.; Zhang, Z.; Mao, S. X. Formation of Monatomic Metallic Glasses Through Ultrafast Liquid Quenching. *Nature* **2014**, *512*, 177−180.

(28) Zhu, T.; Li, J.; Samanta, A.; Leach, A.; Gall, K. Temperature and Strain-Rate Dependence of Surface Dislocation Nucleation. *Phys. Rev. Lett.* **2008**, *100*, 025502.

(29) Stölken, J. S.; Evans, A. G. A Microbend Test Method For Measuring the Plasticity Length Scale. *Acta Mater.* **1998**, *46*, 5109−5115.

(30) Ehrler, B.; Hou, X. D.; Zhu, T. T.; P'ng, K. M. Y.; Walker, C. J.; Bushby, A. J.; Dunstan, D. J. Grain Size and Sample Size Interact to Determine Strength in a Soft Metal. *Philos. Mag.* **2008**, *88*, 3043−3050.

(31) Evans, A. G.; Hutchinson, J. W. A Critical Assessment of Theories of Strain Gradient Plasticity. *Acta Mater.* **2009**, *57*, 1675−1688.

(32) Ashby, M. F. Deformation of Plastically Non-Homogenous Materials. *Philos. Mag.* **1970**, *21*, 399−424.

(33) Zhu, T.; Li, J.; Samanta, A.; Kim, H. G.; Suresh, S. Interfacial Plasticity Governs Strain Rate Sensitivity and Ductility in Nanostructured Metals. *Proc. Natl. Acad. Sci. U. S. A.* **2007**, *104*, 3031−3036.

(34) Hu, T.; Ma, K.; Topping, T. D.; Jiang, L.; Zhang, D.; Mukherjee, A. K.; Schoenung, J. M.; Lavernia, E. J. Disordered Dislocation Configuration in Submicrometer Al Crystal Subjected to Plane Strain Bending. *Scr. Mater.* **2016**, *113*, 35−38.

(35) Greer, J. R.; Nix, W. D. Nanoscale Gold Pillars Strengthened Through Dislocation Starvation. *Phys. Rev. B: Condens. Matter Mater. Phys.* **2006**, *73*, 245410.

(36) Yue, Y. H.; Liu, P.; Zhang, Z.; Han, X. D.; Ma, E. Approaching the Theoretical Elastic Strain Limit in Copper Nanowires. *Nano Lett.* **2011**, *11*, 3151−3155.

(37) Yue, Y. H.; Liu, P.; Deng, Q. S.; Ma, E.; Zhang, Z.; Han, X. D. Quantitative Evidence of Crossover Toward Partial Dislocation Mediated Plasticity in Copper Single Crystalline Nanowires. *Nano Lett.* **2012**, *12*, 4045−4049.

(38) Gu, X. W.; Loynachan, C. N.; Wu, Z.; Zhang, Y. W.; Srolovitz, D. J.; Greer, J. R. Size-Dependent Deformation of Nanocrystalline Pt Nanopillars. *Nano Lett.* **2012**, *12*, 6385−6392.

(39) Jin, M.; Minor, A. M.; Stach, E. A.; Morris, J. W., Jr Direct Observation of Deformation-Induced Grain Growth During the Nanoindentation of Ultrafine-Grained Al at Room Temperature. *Acta Mater.* **2004**, *52*, 5381−5387.

(40) Legros, M.; Gianola, D. S.; Hemker, K. J. *In Situ* TEM Observations of Fast Grain-Boundary Motion in Stressed Nanocrystalline Aluminum Films. *Acta Mater.* **2008**, *56*, 3380−3393.

(41) Shan, Z.; Stach, E. A.; Wiezorek, J. M. K.; Knapp, J. A.; Follstaedt, D. M.; Mao, S. X. Grain Boundary-Mediated Plasticity in Nanocrystalline Nickel. *Science* **2004**, *305*, 654−657.

(42) Colla, M. S.; Amin-Ahmadi, B.; Idrissi, H.; Malet, L.; Godet, S.; Raskin, J. P.; Schryvers, D.; Pardoen, T. Dislocation-mediated Relaxation in Nanograined Columnar Palladium Films Revealed by On-Chip Time-resolved HRTEM Testing. *Nat. Commun.* **2015**, *6*, 5922.

(43) Lu, L.; Shen, Y.; Chen, X.; Qian, L.; Lu, K. Ultrahigh Strength and High Electrical Conductivity in Copper. *Science* **2004**, *304*, 422−426.

(44) Mishin, Y.; Farkas, D.; Mehl, M. J.; Papaconstantopoulos, D. A. Interatomic Potentials for Monoatomic Metals from Experimental Data and *ab Initio* Calculations. *Phys. Rev. B: Condens. Matter Mater. Phys.* **1999**, *59*, 3393−3407.

NOTE ADDED AFTER ASAP PUBLICATION

After this paper was published ASAP on November 22, 2017, a correction was made to the caption of Figure 5. The corrected version was reposted November 28, 2017.